Abstract

The paper focuses on the numerical prediction of the compressive response of masonry by means of detailed micro-modelling techniques. In such a model, the material constituents (mortar and units) and the unit-mortar interfaces are separately described by means of specific constitutive equations.

The available modeling choices are evaluated through a literature review of related case studies. A systematic approach is proposed and is corroborated by the numerical simulation of a large number of experimental cases from various sources. A total of fifty experimental results are simulated resulting in an overall good prediction of the compressive strength and elastic modulus of the masonry composite, as well as a realistic depiction of the failure mode.

This study focuses on the numerical prediction of the compressive strength of masonry, extending to issues pertaining to global stiffness, failure mode, hardening and softening behavior of masonry and their numerical simulation. The masonry typology considered consists of solid units, primarily brick, and mortar of mostly lower strength and higher deformability.

Numerical prediction of the behavior, strength and elasticity of masonry in compression

Anastasios Drougkas[1], Pere Roca, Climent Molins

Departament d'Enginyeria de la Construcció, Universitat Politècnica de Catalunya, Campus Diagonal Nord, Building C1, Jordi Girona 1-3 UPC, 08034 Barcelona, Spain

Highlights

- The behavior of masonry in compression is investigated using micro-models
- A combined smeared cracking-plasticity law is used for the units and mortar
- A total of fifty experimental compression tests are simulated
- Compressive strength and Young's modulus of masonry is well approximated
- Remarks on the behavior and failure mode of masonry in compression are made

Keywords

Micro-modeling, numerical modeling, masonry; compressive strength; Young's modulus; plasticity; smeared cracking

[1] Corresponding Author
Email addresses: anastasios.drougkas@upc.edu (Anastasios Drougkas), pere.roca.fabregat@upc.edu (Pere Roca), climent.molins@upc.edu (Climent Molins)

1. Introduction

Due to the large number of existing buildings composed of masonry structural members such as load bearing walls, the numerical modelling and analysis of masonry structures are receiving at present a growing amount of effort. Masonry buildings are found worldwide and encompass not only a large building stock, still in use, but also valuable architectural heritage.

Given the importance of the seismic action and the potential seismic vulnerability of masonry structures, a significant part of this effort is being devoted to the numerical simulation of masonry failure governed by tension and shear. In particular, the shear failure of masonry walls has been modelled by means of simplified micro-modelling using interface elements to model existing and arising planes of weakness, Lourenço & Rots [1]. Macro-models have also been employed for this purpose, taking into account the orthotropic properties of masonry, Lourenço et al [2], Syrmakezis & Asteris [3] and Pelà et al [4]. Instead, more limited attention has been allocated to the detailed simulation of the masonry response and failure in compression. However, an accurate characterization of the compressive strength of masonry is needed in order to verify the capacity of masonry structures subject to both vertical and horizontal actions, both of which activate compressive struts in masonry members. In meso-models and simplified micro-models the compressive strength of masonry is given a value by the analyst a-priori.

Several attempts of simulation of the compression behavior of masonry have been undertaken using three-dimensional models with varying purposes and results. This behavior, governed by the interaction of the units and the mortar, may be strongly affected by out-of-plane effects, as analytical models have indicated, Hilsdorf [5]. One of the first numerical attempts involved a set of elastic analyses on hollow concrete block masonry under concentric compression, Hamid & Chukwunenye [6]. A similar parametric analysis was conducted to study the influence of elastic properties and joint dimensions on stress distribution and masonry elasticity, Reddy et al [7]. The differences between plane stress, generalized plane strain and three-dimensional modeling of masonry in terms of strength, elasticity and stress distribution have been discussed, Anthoine [8].

Similar observations have been made using nonlinear models in order to comment on the effects of model geometry on the predicted compressive strength of masonry, Berto et al [9], Barbosa et al [10]. Finally, the

general deficiencies of plane models in accurately reproducing the behavior of single- and multi-leaf walls in numerical analyses have also been noted by Milani et al [11,12]. According to the latter authors, 3D effects need to be taken into account for the correct derivation of the failure envelope of masonry under in-plane loads. Additionally, other case studies include the simulation of concentric, Furtmüller & Adam [13], Schlegel [14], Vyas & Reddy [15], and eccentric compression of masonry, Adam et al [16], Brencich et al [17]. Finally, three-dimensional periodic unit cells have been used for the verification of the results of homogenization methods for masonry under triaxial normal and shear stress, Cecchi et al [18], Zoucchini & Lourenço [19].

Application of modeling approaches proposed for the study of masonry in compression has been rather narrow in scope, normally extending to only a very small number of experimental cases each. This fact also narrows the capacity for comparison between the results of experiments, empirical expressions and numerical results concerning the compressive strength of differing types of masonry.

The purpose of the modeling strategy presented herein is found in the detailed simulation of the failure of masonry under compressive loading by means of a general approach combining versatility (the ability to analyze a variety of cases regarding geometry and material constituents) and a moderate computational cost. The strategy is based on detailed micro-modelling where specific constitutive equations are used separately for the material constituents (mortar and units) and the unit-mortar interfaces.

The applicability of the method focuses on masonry prisms and walls consisting of solid bricks and mortar arranged in stack bond, running bond and Flemish bond walls and in English bond pillars. In principle, this approach can be applied to any type of masonry bond, since geometrical peculiarities are taken into account explicitly in the model geometry. Adopting a detailed micro-modeling approach for the simulation of failure in masonry means that, in principle, geometry and morphology of the structure should not be a limiting factor as long as the phenomena affecting strength, elasticity and failure initiation and development are modeled accurately.

The modeling approach has been tested against existing experimental data, focusing exclusively on case studies where sufficient material characterization has been carried out. In this research, a total of fifty different experiments have been simulated. Micro modeling requires knowledge of several elastic and strength

parameters, many of which are usually not measured in experimental campaigns, the Young's moduli being a case in point. The analyses carried out in this report and their comparison with the experimental data may contribute to the enrichment of the inventory of numerical results on the analysis of masonry structures and provide a starting point for further investigation through parametric and sensitivity analyses.

Most of the case studies encountered in the literature and actually adopted for the present research involve units stronger than the mortars. This leads to compressive failure modes governed by crushing of the mortar under multi-axial compression and cracking of the units under combined compression and tension.

The proposed numerical approach can be applied to masonry with typical combinations of materials and structural arrangements, but is especially suited for the analysis of traditional brick masonries composed of lime mortars of low compressive strength. Modern brick masonries, built with cement mortar of a compressive strength close to or higher than that of the bricks may require a different approach. The applicability of the method is further discussed in section 5. The numerical analyses have been performed using the finite element program DIANA [20].

2. Material Models

General

The compressive strength of masonry is determined by, among other factors, the properties of its constituent materials. According to empirical expressions, such as the one found in [21], it is estimated by the compressive strength of both the units and the mortar, normally assuming the former is higher than the latter. The resulting strength of the composite lies between the two values, implying that the mortar fails under a stress level higher than its uniaxial compressive strength.

Furthermore, the failure mode commonly encountered in masonry in compression, aside from the crushing of the joints, is vertical cracking of the units, caused by the lateral expansion of the mortar in the joints. Failure at the unit-mortar interface in horizontal, vertical and transversal joints occurs by way of separation under tension, especially in the vertical and transversal joints, and shear slipping.

Therefore, detailed micro-modeling approaches for the simulation of masonry need to be able to model the nonlinear behavior of the units and the mortar in tension leading to cracking and pressure dependent behavior under multi-axial compression. Tensile and shear failure at the unit mortar interface need to be modeled as well. Thus the failure of the structure in both arising and macroscopically existing planes of weakness needs to be accounted for.

For the present research, the numerical analyses have been performed using a mixed pressure dependent plasticity model in compression and a smeared cracking model in tension, organically combined in a total strain non-linear model with secant unloading [20,22]. Therefore, it is possible to simulate all failure modes normally expected to arise in masonry under compression.

Damage due to tensile cracking is modeled using a rotating crack model, in which stress-strain relationships are evaluated in the principal directions of the strain vector. The direction of the cracks may therefore change according to the direction of the principal strain.

Shear behavior is explicitly governed by a relationship between shear stress and shear strain, while six internal damage variables α_k (assembled in the $\boldsymbol{\alpha}$ vector), indicating the ratio of damaged to effective stress, monitor the deterioration of the material, which is non-recoverable.

This constitutive law has been used in numerical simulations for concrete and masonry macro-models. It may be considered an attractive choice for the simulation of masonry since it is capable of modeling its behavior in compression, tension and the interaction of the failure modes.

Tensile Behavior

The stress-strain relationship is elastic until the tensile strength is reached. The expression of the tensile behavior in the post-peak using values for the tensile strength f_t and the tensile fracture energy G_f^I is accomplished through the use of an exponential softening curve. For the post-peak of the tensile stress-strain relation, the damaged stress is expressed as:

$$\sigma(\varepsilon_{cr}) = f_t e^{-\frac{\varepsilon_{cr}}{\varepsilon_{cr,u}}} \qquad (1)$$

where ε_{cr} is the crack strain and $\varepsilon_{cr,u}$ the ultimate crack strain. To calculate $\varepsilon_{cr,u}$ the softening equation is rewritten as:

$$\sigma(\varepsilon_{cr}) = f_t y\left(\frac{\varepsilon_{cr}}{\varepsilon_{cr,u}}\right) = f_t y(x) \tag{2}$$

According to the definition of the tensile fracture energy:

$$G_f^I = h\int_{\varepsilon_{cr}=0}^{\varepsilon_{cr}=\infty} \sigma(\varepsilon_{cr})\, d\varepsilon_{cr} = f_t h\left(\int_{x=0}^{x=\infty} y(x)\, dx\right)\varepsilon_{cr,u} \tag{3}$$

Therefore, the ultimate crack strain is:

$$\varepsilon_{cr,u} = \frac{G_f^I}{f_t \cdot h} \tag{4}$$

A crack bandwidth equal to a characteristic dimension given by $h = \sqrt[3]{V}$ is adopted, where V is the volume of the finite element. Snap-back is avoided if the absolute initial slope of the softening diagram for the given crack bandwidth is lower than the initial tangent Young's modulus. This holds for:

$$h \le \frac{G_f^I E}{f_t^2} \tag{5}$$

where E is the initial tangent Young's modulus.

Finally, cracked directions subjected to tension are not affected by the Poisson effect, meaning that such loading does not lead to contraction in the perpendicular directions. Therefore, an orthotropic formulation has been adopted for the Poisson's ratios, which are reduced at the same rate as the secant modulus after cracking [22].

Due to the rotating crack assumption, the crack orientation follows the direction of the principal stress. Therefore, retention of shear stiffness in the crack need not be modeled.

Compressive Behavior

Uniaxial unconfined compressive behavior is modeled using a parabolic compression curve based on fracture energy [23]. The curve is defined by three characteristic strain values: the strain for which hardening is initiated at one third of the compressive strength, the strain for which maximum stress is reached and the strain for which softening is terminated. For a uniaxial compressive strength f_c and an initial tangent modulus of E, the strain $\varepsilon_{c/3}$, at which one third of the compressive strength has been reached, is expressed as:

$$\varepsilon_{c/3} = -\frac{1}{3}\frac{f_c}{E} \tag{6}$$

The strain ε_c, at which the maximum compressive strength is reached, and is expressed as:

$$\varepsilon_c = -\frac{5}{3}\frac{f_c}{E} = 5\ \varepsilon_{c/3} \tag{7}$$

The ultimate strain ε_u, at which the material has terminated its softening in compression, which is expressed as:

$$\varepsilon_u = \varepsilon_c - \frac{3}{2}\frac{G_f^c}{h\, f_c} \tag{8}$$

where, in turn, G_f^c is the compressive fracture energy and h is the characteristic element length. In addition to the mesh insensitivity of the model, strain localization and dissipation of the compressive fracture energy is ensured by the geometry of the models themselves given that compressive damage is normally expected to occur in the mortar joints. The parabolic compression curve is defined for strain ε by the piecewise equation:

$$f = \begin{cases} -f_c \dfrac{1}{3}\dfrac{\varepsilon}{\varepsilon_{c/3}} & \text{if } \varepsilon_{c/3} < \varepsilon \le 0 \\ -f_c \dfrac{1}{3}\left(1+4\left(\dfrac{\varepsilon-\varepsilon_{c/3}}{\varepsilon_c-\varepsilon_{c/3}}\right)-2\left(\dfrac{\varepsilon-\varepsilon_{c/3}}{\varepsilon_c-\varepsilon_{c/3}}\right)^2\right) & \text{if } \varepsilon_c < \varepsilon \le \varepsilon_{c/3} \\ -f_c\left(1-\left(\dfrac{\varepsilon-\varepsilon_c}{\varepsilon_u-\varepsilon_c}\right)^2\right) & \text{if } \varepsilon_u < \varepsilon \le \varepsilon_c \\ 0 & \text{if } \varepsilon \le \varepsilon_u \end{cases} \tag{9}$$

Lateral pressure dependence, which accounts for increased strength under confining stress, has been modeled using the four parameter Hsieh-Ting-Chen failure surface [22,24], which is defined as:

$$f = C1\frac{J_2}{f_c^2} + C2\frac{\sqrt{J_2}}{f_c} + C3\frac{f_{c1}}{f_c} + C4\frac{I_1}{f_c} - 1 = 0 \tag{10}$$

where I_1 and J_2 are the stress invariants and f_{c1} is the maximum principal stress. The numerical values of the material parameters *C1*, *C2*, *C3* and *C4* are determined by uniaxial compression, uniaxial tension, equal biaxial compression and triaxial compression tests on the material in question. All the stresses in the criterion are normalized by the uniaxial compressive strength, implying that the behavior described by the model may be applied to materials of different strength but similar behavior. The stress f_{c3}, a negative stress value which results in compressive failure, is determined by scaling the linear elastic stress vector $\sigma_c = sE\varepsilon_{nst}$ such that equation (10) holds, where s is the scaling factor sought, E the tangent Young's modulus and ε_{nst} the principal strain vector. Thus, f_{c3} is defined as the minimum normal stress component of the stress vector. The confined compressive strength is expressed as $f_{cf} = -f_{c3}$ and its ratio to the uniaxial compressive strength is expressed as $f_{cf} = K_\sigma f_c$. The peak strain factor, relating peak to initial strain ($\varepsilon_P = K_\sigma \varepsilon_0$) is equal to the ratio between confined and uniaxial compressive strength.

The peak stress is obtained by taking into account the influence of lateral cracking. This influence on the compressive behavior is modeled using a reduction factor [25]. The reduction factor, denoted as $\beta_{\sigma_{cr}}$, is a function of the average lateral damage variable given by $\alpha_{\text{lat}} = \sqrt{\alpha_{l,1}^2 + \alpha_{l,2}^2}$, where $\alpha_{l,1}$ and $\alpha_{l,2}$ are the two damage variables, obtained from the $\boldsymbol{\alpha}$ vector in the two lateral to the compressive load directions, and is calculated by:

$$\beta_{\sigma cr} = \frac{1}{1 + K_c} \leq 1 \tag{11}$$

where:

$$K_c = 0.27\left(-\frac{\alpha_{\text{lat}}}{\varepsilon_0} - 0.37 \right) \tag{12}$$

Finally, the peak stress is given by:

$$f_{\text{P}} = \beta_{\sigma_{cr}} \cdot f_{cf} \tag{13}$$

The initial strain ε_0 is given by the equation:

$$\varepsilon_0 = -\frac{n}{n-1}\frac{f_c}{E} \tag{14}$$

with:

$$n = 0.80 + \frac{f_{\text{P}}}{17} \tag{15}$$

Increase in ductility due to lateral confinement is modeled according to the following stress-strain expression:

$$f = -f_P\left(1 - (1-r)\frac{\varepsilon - \varepsilon_{\text{P}}}{\varepsilon_U - \varepsilon_{\text{P}}} \right) \leq -f_{cr} \tag{16}$$

assuming a value for the ultimate strain:

$$\varepsilon_U = \left(\frac{f_P}{f_c} \right)^3 \varepsilon_P \tag{17}$$

The residual compressive strength f_{cr} is expressed as:

$$f_{cr} = f_c r \tag{18}$$

Where:

$$r = 0.1 \left(\frac{f_P}{f_c} \right)^3 \tag{19}$$

A comparison of the basic parabolic curve for uniaxial compressive loading and its comparison to a curve under lateral compression is presented in Figure 1.

Interface Behavior

Unit-mortar interface behavior is described using a discrete cracking model based on a total deformation theory, in which interface tractions are expressed as a function of the total relative displacements [20].

Elastic behavior is assumed until the traction reaches the assigned tensile strength and a brittle behavior is assumed post-peak: normal stiffness is reduced to zero. Therefore, normal tractions t_n are expressed as:

$$t_n = \begin{cases} k_n \Delta_n & \text{if } \Delta_n \leq f_{t,i}/k_n \\ 0 & \text{if } \Delta_n > f_{t,i}/k_n \end{cases} \tag{20}$$

where k_n is the normal interface stiffness, $f_{t,i}$ is the interface tensile strength and Δ_n is the interface relative displacement.

It is assumed that shear stiffness of the interface reduces to zero after the onset of cracking, by adopting a shear retention factor of zero.

3. Modeling

Geometry

A body of work involving detailed modeling of masonry under in-plane loads, in which units and mortar are modeled separately, has been produced [8–10]. In these cases, the unit-mortar interaction results in out-off-plane stresses which may significantly alter the compressive behavior of the masonry composite. This is especially true in cases where there is significant discrepancy between the elastic characteristics of the two constituent materials, namely the Young's modulus and the Poisson's ratio.

It is appealing from the point of view of computational cost and modeling effort to model wall structures, such as running or Flemish bond masonry using simple plane geometrical models, such as plane stress or plane strain. However, the results obtained demonstrate some patterns of divergence from experimentally observed behavior and obtained compressive strength. In plane stress analyses the units afford very low confinement to the mortar, while in plane strain analyses the confinement is excessive. The results of the under- and over-estimation of the effects of unit-mortar interaction in these cases are, expectedly, too low compressive capacity in the former and too high compressive capacity in the latter. The failure modes are also characteristic of the above modeling approaches, in plane stress more so than in plane strain, with the former leading to excessive yielding in compression of the weakest material and with the latter usually leading to excessive cracking of the strongest and stiffest. The issue of directly modeling the non-constant geometry of, for example, Flemish bond walls and English bond columns raises further doubts concerning the adequacy of plane methods. Figure 2 illustrates various masonry typologies of different degrees of geometrical complexity.

The regular assumptions accompanying plane analysis methods are not sufficient due to the geometrical layout of the masonry composite. The ratio of the thickness of the mortar joints, which is of the order of 10 *mm*, over the thickness of the masonry, which is of the order of 100 *mm*, invalidates the plane stress assumption of zero thickness. This dimension ratio results in out-off-plane effects, and stresses, to become locally significant near failure even though the assumption is conceptually sound on a global, structural level. Similarly, the assumption of infinite masonry thickness certainly does not hold globally, though it may be a legitimate simplification for local effects given the usual ratio of dimensions mentioned above. Generalized plane strain,

although maintaining some elements of phenomenological modeling, is usually a closer approximation of the actual behavior and leads to better results for the simulation of local failure [26,27].

Overall, the more homogenous the composite is, implying units and mortar of similar properties, plane stress becomes more accurate, while plane strain becomes more accurate for increasing property disparities between the two material phases. The two plane methods should generally provide accurate results for extreme or particular cases, but their capacity to provide accurate results for intermediate or general cases has not been demonstrated.

Three-dimensional micro-modeling, while computationally the most demanding approach, has been shown to produce the consistently most accurate results in terms of capacity when applied to a large number of different experimental cases. No geometrical assumptions are made and, therefore, out-off-plane effects and stresses are taken into account organically, both on the structural and on the local level, thus allowing the modelling of masonries with a variety of different geometrical textures. Vertical and horizontal compressive strength values obtained using this method fall between those obtained from plane stress and plane strain. Overall, the comparison with available experimental data is favorable compared to that of plane methods. Interestingly, all the above mentioned modeling approaches produce equal initial stiffness in compression for the masonry composite. Figure 3 illustrates examples of three-dimensional models, including the overall layout and the distribution of stress under vertical loading.

In the present work the models are composed of 20-node isoparametric solid elements based on quadratic interpolation and 3x3x3 Gauss integration scheme [20]. The fineness of the mesh was adjusted accordingly as to include at least two elements along the thickness of each joint. Symmetric loading of symmetric structures allows for three planes of symmetry to be applied, thus greatly reducing the size of the models.

The unit-mortar bond was modeled using a discrete cracking law applied on zero thickness 8+8 node plane quadrilateral interface elements, based on quadratic interpolation and a 4x4 Newton-Cotes integration scheme [20].

Solution Method and Loading

The analysis procedure for the solution of the physically non-linear problem was the Modified Newton-Raphson method. A Line Search algorithm was used to predict the iterative displacement increment and to speed-up the convergence rate.

The loading was prescribed in displacement control. An energy based convergence criterion was used for the convergence check, since displacement loading reduces the usefulness of the displacement norm criterion and the, mostly, unrestrained lateral expansion of the models reduces the buildup of internal forces, thus making the force norm less useful. For the convergence criterion a 0.5% energy norm was adopted.

The finite element code DIANA, in which the above constitutive laws and element types are implemented, was used for the analyses, employing a parallel direct sparse solver [20].

4. Inventory of Experimental Result Data

Overview

There is a relatively large inventory of existing experimental data on masonry compression. However, the number of those qualifying for a numerical reproduction using micro-models is fairly limited. The cause of this is the lack of sufficient material characterization. Parametric analysis performed in this research has indicated a clear, if rather strong, influence of the Young's modulus of both units and mortar on the compressive capacity and the failure mode observed. Difficulties in measuring the Young's moduli of small size specimens, coupled with the reliance on empirical expressions for the determination of the strength of the composite based solely on the compressive strength of the two constituents [21], have brought about a lack of motivation for taking adequate measurements of it, especially in the case of mortars, despite observations on the effect of the deformation properties of the masonry constituent materials on the behavior of masonry composites [28–30]. Tensile strength measurements are also often neglected in unit characterization, even though unit cracking is commonly observed in compression of masonry.

Certainly, there exists a strong correlation between the compressive strength and the Young's modulus or the tensile strength, especially in modern types of units. However, the validity of a direct correlation between

the two values is less clear for masonries built with low strength mortars (such as traditional lime mortars) where other factors, such as composition and ageing, may affect significantly on the resulting masonry stiffness.

In summary, the available candidate case studies for numerical simulation are few in number and mostly concerning stack bond prisms [7,13–17,31–41]. Case studies of walls in running bond are not uncommon [33,40,42–44] but tests on walls in Flemish bond are rare [45] while a few suitable examples of English bond pillars were also identified [13,33]. The vast majority of these cases involve the characterization of clay brick masonry with a few exceptions involving stone block masonry [14,35] or compressed cement block masonry [15]. All mortars were either cement or lime/cement mortars, with one exception where pure lime mortars were used [32].

The average ratio of Young's modulus to compressive strength is 328 for the units, with values ranging from 14 to 1265. The average for the mortars was 699, with values ranging from 22 to 2094. The average for the masonry was 356, with values ranging from 29 to 1903. The highest figure corresponds to the only case with a ratio above 1000 while the remaining values, and their average, are much lower than 1000, which is the characteristic value recommended by design codes (e.g. [21]).

Assumed Values

The dimensions, compressive strength and Young's modulus of the units and mortar were reported in all the examined cases, with the exception of one case in which the Young's modulus of the mortar was calculated in this study using the values given for the units and the masonry composite.

In order to perform the analyses of the available case studies, it was necessary to assume values for the missing parameters. The available literature overviewed in the present work offers an adequate amount of information on which to base these assumptions.

The average value of the measured Poisson's ratio in the set of case studies is 0.13 for the units with values ranging from 0.07 to 0.24 while for the mortars it is equal to 0.15 with values ranging from 0.07 to 0.2. In the cases where it was not reported, the Poisson's ratio for the units was chosen as being equal to 0.15 while a value between 0.15 and 0.25 was chosen depending on the type of mortar. In [32,38] a weak lime mortar was used, so

a value of 0.25 was adopted. For [31,33,37,40,43], for which a cement/lime mortar was used, a value of 0.20 was adopted. In [34,36] Portland cement mortars were used and a value of 0.15 was used.

The average ratio of tensile to compressive strength for the units was 9% with values ranging from 1.8% to 23.9%. For the mortar the average was 8.2% with values ranging from 5% to 26%. For all the mortars a ratio of 10% was assumed for the missing values. In the case of the units the ratio differed from case to case depending on the material used and the workmanship employed. For [33] and [37] a ratio of 10% was used since they involved wire cut solid clay bricks. The average value of all solid clay bricks in the inventory had an average ratio of 9.3%. This value is similar to the 10% usually assumed for masonry units. In [34] a ratio of 5% was assumed since the campaign was performed using hand molded bricks. This lower percentage was assumed in order to reflect the poorer quality and consistency of hand-made bricks compared to machine molded bricks. In [7] soil-cement blocks were constructed, therefore a 5% ratio was adopted. For [35], which involved granite units, a ratio of 5% was chosen. According to [46] this is a ratio that fits the available experimental data on granites well.

The plasticity and cracking models require values for the compressive and mode-I fracture energies in order to describe the softening behavior of the materials. The current status of the research on these values for clay bricks and, especially, lime mortars is quite limited. Only a small number of the cases in the experimental inventory include values for the compressive and tensile fracture energy of the units and/or the mortar. The values for the fracture energy of the units and the mortar were determined using equations (21) and (22). The compressive fracture energy of both the units and the mortar was calculated assuming a ductility index parameter of 1 *mm*, defined as

$$d = G_f^c / f_c \tag{21}$$

while the tensile fracture energy was calculated according to the following equation:

$$G_f^I = 0.025\left(2 f_t\right)^{0.7} \tag{22}$$

which is based on the equation provided for the calculation of the tensile fracture energy by CEB-FIP Model Code 1990 [47] adjusted to assume a ratio between tensile and compressive strength of 5% and a maximum aggregate size of 8*mm*. The wide range of mortar and unit materials used in masonry and the lack of information concerning the values for their fracture energy necessitates the adoption of the above rather conservative values.

Very few of the experimental cases provide any measurement of the unit-mortar interface properties. Furthermore, only a small number of works focused on these properties exists [48,49] which can hardly be used as a general guideline in a study of this extent. Therefore, representative values had to be assumed. Throughout the cases a tensile strength of 0.2 *MPa* was considered, while zero Mode I fracture energy (brittle cracking) and zero shear retention after the formation of the crack were assumed. Prior to failure the bond is considered perfect, therefore a large initial elastic stiffness was considered in the normal and perpendicular directions of the interface, meaning that virtually all deformation in the interface is nonlinear.

The numerical parameters *C1*, *C2*, *C3* and *C4* were taken as being equal to 2.0108, 0.9714, 9.1412 and 0.2312 respectively. These values correspond to a tensile strength equal to 10% of the compressive strength, a biaxial compression strength equal to 1.15 times the uniaxial and a compressive strength under biaxial pressure equal to 80% of the compressive strength equal to 4.2 times the uniaxial strength. All four tests necessary for the complete determination of the four parameters are practically never available for mortars used in masonry. This problem is compounded in the case of existing masonry structures, where material sampling for all four tests is very difficult. The problem is less crucial in the case of masonry units, either clay or stone, since the behavior of masonry is not influenced by the pressure dependent behavior of the units in compression. Since the failure mode in tension is governed by the smeared cracking model, the determination of the ratio of tensile to compressive strength is not crucial.

5. Results

Presentation of Results

The cases available for numerical analysis include thirty-one stack bond cases (S), nine running bond masonry cases (R), three Flemish bond masonry cases (F) and seven English bond pillar cases (P) for a total of

fifty cases. The cases for each bond type have been sorted and numerically named in ascending order according to their statistical fit with the experimental compressive strength.

The material properties and dimensions for the models were taken as reported in the experimental results and are shown in Tables 1 through 4. The values assumed as mentioned above for unknown quantities are displayed in brackets. Examples include several Poisson's ratios and values for the tensile strength. The experimentally achieved values, along with the numerical value for the compressive strength, are also shown in the same table.

Computational effort remains substantial but not excessive: a single small or medium sized wall may be analyzed in order to obtain the maximum load and part of the post-peak curve in two to three hours using a conventional PC. The attainment of the full post-peak curve may cause computational time to double.

Analysis of Results

With a few exceptions, the modeling strategy produced adequately accurate predictions of the compressive strength throughout the group of cases, which includes a wide range of material combinations. Certain experimental results may be regarded as dubious, such as S29 and S24, where the compressive strength was too high and too low respectively, considering the strength of the materials and the dimensions reported. Others, such as F3, were executed using extremely strong and stiff mortar and should be seen as outside the intended scope of this modeling approach.

The accuracy of the method regarding the determination of the Young's modulus of masonry is comparably high. However, certain cases such as F1, F2 and F3 exhibited an experimental elastic modulus much lower than what would be expected considering the elastic moduli provided for the constituents.

Figure 4 illustrates the relation between numerical and experimental values of the compressive strength, showing a good agreement between the experimental and the numerical results. Throughout all cases the coefficient of determination was 0.969 for the numerical prediction. Similarly, Figure 5 illustrates the relation between the numerical and experimental values of the Young's modulus of the masonry composite in vertical compression. Throughout the cases the coefficient of determination was 0.892. The ratios of masonry Young's modulus over the compressive strength are roughly equal to the ones produced by the experimental results.

Concerning the comparison of the numerical and experimental results, certain comments should be made regarding the applicability of the proposed method. As has been previously stated, the method is intended to be applied in cases of units with higher compressive strength and lower deformability than the mortar. All of the examined cases comply with this intention, with the exception of the F3 case, involving a mortar that is three times as strong in compression as the bricks, and the S6 case, in which the two components have equal strength.

Some remarks must be also made with regard to a few experimental measurements that do not comply with the general trend of the full inventory of experimental cases considered. These cases, labelled S6, S21, S23, R8, F3 and P6, are the only ones for which the compressive strength of the composite is lower than that of both constituent materials (mortar and units). This low compressive strength cannot be correctly predicted using this analysis method as can also not be accounted for by usual models for predicting the compressive strength of masonry. Finally, the Poisson's ratio reported for the mortar in the F1 case, a pozzolana-lime mortar with low strength, is very low compared to the average derived from the experimental inventory. A higher value for this parameter, which would increase the amount of confinement on the mortar layers, would result in an increase in the numerically predicted masonry compressive strength. Disregarding the above mentioned cases increases the coefficient of determination for the prediction of compressive strength to 0.976.

The dominant failure mode obtained was a combination of mortar yielding in compression and unit cracking for the majority of the cases. Two major types of secondary damage were registered. Firstly, some initial cracking of the mortar at the unit-mortar interface near the outer faces of the masonry. Secondly, compressive yielding of the units in the case of masonries with mortar stronger in compression than the units. The observed failure modes will be discussed in the following paragraphs, with some emphasis on their dependence on material properties.

Great discrepancy between the elastic characteristics of the units and the mortar enhances the confinement afforded on the mortar, resulting in a higher ratio between the masonry compressive strength and the mortar compressive strength. Therefore, the relation between the compressive strength of the constituents and the compressive strength of the composite is partly dependent on the Young's moduli as well, especially in cases where the global failure mode is governed by mortar yielding in compression.

Compressive yielding mainly takes place in the mortar joints. Crushing failure of the mortar, represented numerically by plastic strains, normally initiates near the face of the masonry, where horizontal confinement is lowest, and develops towards the interior of the joint. In the running bond and Flemish bond wall cases, this compressive yielding failure exhibited a repeating pattern across the face of the structure, both in the horizontal and the vertical joints. Lateral expansion of the crushed mortar causes cracking damage in the units at the interface near the free surface of the masonry. The non-uniform development of compressive damage along the depth of the horizontal joints indicates that plane methods, as already discussed, may be inadequate for an accurate description of the phenomenon. The development of mortar yielding is illustrated in Figure 6.

Compressive yielding of the units to an extent that affects the global failure mode only occurs in cases of very strong mortar. For mortars with compressive strength comparable to or higher than that of the units, compressive yielding of the units may occur in the pre-peak range and initiate overall failure.

Notable compressive yielding of the units may also take place after extensive cracking, covering nearly the entirety of the unit. This only happens far in the post-peak and does not affect the stress-strain curve near the peak.

Cracking damage mainly takes place in the units and the head and transversal joints. The appearance of extensive cracking in the units, represented numerically by crack strains, and its influence on the global failure, are not directly dependent upon the ratio of the Young's moduli. For high ratios, lateral tension on the units increases but the onset of extensive unit cracking may not necessarily occur before the yielding of the mortar.

The amount of vertical confinement afforded on the mortar and the amount of vertical splitting on the units are directly dependent on the mismatch of elastic properties of the constituent materials. The prevalence of one of the two failure modes over the other depends on both the elastic and inelastic properties.

Overall, the numerically obtained failure mode is chiefly governed by mortar compressive yielding which develops during the hardening of the structure. The compressive strength of the units does not appear to play a direct role in the compressive strength of the composite for the majority of the cases. Unit compressive yielding is not involved in the initiation of failure; conversely, tensile unit strength is more directly involved, especially

in the post-peak. Cracking of the units near the unit-mortar interface initiates in the outer surface of the masonry and remains superficial without extending towards the interior of the masonry. The more critical vertical cracks in the units may extend into the interior of the masonry in the post-peak, a further indication that plane analysis methods are inadequate. The development of cracking in the units is illustrated in Figure 7.

A comparison of experimentally and numerically derived stress-strain curves is presented in Figure 8, covering a wide range of results in terms of compressive strength and elastic stiffness. The graphs show the good agreement obtained between the initial Young's modulus of masonry as measured in the experiments and that predicted by the numerical model. The numerical post-peak curve is usually steeper, as in graphs (c) and (f). This is an indication that the values assumed for the tensile fracture energy of the units and/or the compressive fracture energy of the mortars is low. However, some of the experimental case studies were, indeed, characterized by such steep softening, a behavior which was well approximated in the numerical model, as shown in graphs (a) and (f).

Concerning the missing material parameters, the absence of values for the tensile strength of the mortar is of very small consequence for the determination of the compressive strength of masonry. However, the tensile strength of the units plays a more substantial role, as demonstrated by the cracking development near and after the load peak. The Poisson's ratio of the mortars with low Young's modulus is also a strong influencing factor as it affects the lateral expansion of the mortar under vertical compression and, therefore, the amount of horizontal confinement afforded to it by the units. It can be thus concluded that the tensile strength of the units and the Poisson's ratio of the mortar are of importance in masonry in compression and their function is linked.

In the majority of cases where a relatively high Poisson's of 0.2 was assumed the model exhibited a tendency to slightly overestimate the compressive strength of masonry. This is especially apparent in the cases from [33], [38] and [43]. A value of 0.15, which is closer to the average, would have resulted in a slightly better estimation of the compressive strength of masonry.

For comparison purposes, analyses of the running and Flemish bond cases were performed without taking into account nonlinearities in the interface elements (meso-modeling). The resulting compressive strength was identical to the one obtained from the detailed micro-models, despite the fact that the meso-models could not

take into account tensile failure of the interfaces between the units and the head and transverse mortar joints simulated by the micro-models.

Similarly, the influence of the tensile strength of the mortar was investigated in the F1 Flemish bond case while at the same time neglecting interface nonlinearities. The existence of both head and transversal mortar joints potentially maximizes the influence of this particular material parameter. Cracking in the mortar occurs very early in the analysis, appearing in all vertical, transversal and horizontal joints. In the former two cases the damage propagates through the entirety of the joint, while in the latter the damage is limited to an area near the surface of the masonry, which is also the first to fail in compression. However, in terms of overall behavior, the strength and the elasticity of the masonry composite are not significantly altered by the modification of the tensile strength of the mortar: using a value of 10% and 1% of the experimentally derived value of the tensile strength of mortar caused a reduction of only 2.1% and 3.6% of the compressive strength of masonry.

The sensitivity of the results to the fineness of the mesh was studied on the S1 experimental case [41]. Three meshes were employed, the defining parameter for refinement being the number of elements along the thickness of the joint. In the main series of numerical analyses performed in this paper, two elements were used along the thickness of the joint. Two additional meshes were tested: one with a single element and one with three elements along the thickness. The aspect ratio of the resulting finite elements are 1:0.93:0.92, 1:0.62:0.92 and 1:0.41:0.92 for the three cases.

The results are presented in Figure 9. While the compressive strength and initial axial stiffness was unaltered, there is a distinct influence of the fineness of the mesh in the post-peak. The model with a single element across the joint exhibits a more ductile behavior. The results of the two and three element models exhibit similar post-peak behavior.

Overall, mesh refinement only affected the post peak behavior but not the predicted capacity. The coarser mesh resulted in a more ductile response. Finally, there was very little benefit in using three instead of two element along the thickness of the joint.

Comparison with Closed Form Expressions

The numerical results are compared with a number of closed form and empirical expressions for the prediction of the compressive strength of masonry and its Young's modulus. These analytical expressions are applied to those cases where the masonry materials are completely characterized, with the occasional exception of the value of the tensile strength of the mortar, which does not influence the results for any of the analytical models or for the FEM analyses.

The analytical models proposed by Hilsdorf [5], Khoo & Hendry [50], Francis [51], Ohler [52] and Hendry [53] are used, as well as recommendations by ACI [54] and CEN [21] standards for the characteristic strength of masonry. The elastic modulus of the composite as derived from a simple one-dimensional homogenization method [55] and the CEN European standard are similarly compared with the experimental and numerical results.

The results for the compressive strength and the Young's modulus are summarized in Table 5 and Table 6 respectively. The Ohler and Hilsdorf models are the most accurate, producing results of comparable accuracy to the numerical model. They are followed by the Khoo & Hendry, Francis and Hendry models. However, most models produce a compressive strength higher than the compressive strength of the unit for a number of cases, such as the Hendry model for cases S13, R9, F1, F2 and F3, the Francis model for cases S18, S20, S28, F2 and F3 and the Khoo & Hendry and Hilsdorf models for case F3. The equations provided by the design codes tend to underestimate the compressive strength, especially for masonry composites of higher strength, with the values provided by CEN being slightly closer to the experimental results. The FEM model provides, with a few exceptions, results for the Young's modulus very similar to the analytical model. The CEN code tends to greatly overestimate this parameter compared to the experimental results.

6. Conclusions

A systematic numerical simulation of masonry compression tests has been performed on fifty cases with available experimental results using a detailed micro-modeling technique. The main purpose of the simulation has been the validation of the proposed micro-modeling technique for the prediction of the compressive strength and elastic modulus of masonry based on the properties of the constituent materials.

The modeling method, resulting from the application of a combined plasticity and smeared cracking material law in three dimensional masonry models has been shown capable of producing reliable results in a wide range of combinations of masonry units and mortar. Its accuracy, however, is strongly dependent on sufficient mechanical characterization of the individual materials and should be tested against carefully executed tests on the resulting masonry. Overall, no distinct tendency to over- or underestimate the compressive strength and elastic modulus of the masonry was observed.

The range of applicability of the proposed technique is far greater than that of plane methods (such as plane strain or plane stress applications), as unit-mortar interaction and its out-off-plane effects differ greatly for different ratios of elastic moduli between the materials. Three-dimensional micro-models allow a more accurate and general simulation of the masonry compressive effects due to the more realistic prediction of damage patterns and their development.

In summary, the simulation of phenomena associated with masonry compressive effects using micro-models is much more accurate and of wider applicability when using models of three-dimensional geometry due to the more realistic prediction of damage patterns and their development. Abiding to the principle aims of structural micro modeling, which include the direct, rather than the phenomenological, simulation of structural behavior and failure, and in an effort to establish a generally applicable modeling approach, three-dimensional micro-modeling appears to be the most promising and advantageous method.

The numerical results have been compared with a number of closed form and empirical expressions for the estimation of the masonry compressive strength and Young's modulus. Compared to the closed form and empirical expression, the numerical model provides far more accurate estimations. In fact, some of the expressions tested provide only fair estimations. A significant discrepancy has been found between the equation proposed by CEN 2005 [21] for the estimation of the Young modulus and the experimental or numerically predicted results. According to the comparison, the equation of CEN 2005 largely overestimates the Young's modulus.

A particular application of the proposed numerical approach can be found in the estimation of masonry average properties based on the knowledge of specific parameters of the material constituents. These properties

may be later used as input data for macro-models utilized in the analysis of large structural parts or entire structures.

ACKNOWLEDGMENTS

This research has received the financial support from the *Ministerio de Educación y Ciencia* through the research project SUBTIS (*Study of the Sensitivity of Urban Buildings to Tunneling Induced Settlements*, ref. num. BIA2009-13233), the project MICROPAR (*Identification of mechanical and strength parameter of structural masonry by experimental methods and numerical micro*-modeling, ref num. BIA2012-32234) and the ERDF (*European Regional Development Fund*).

References

[1] Lourenço PB, Rots JG. Multisurface interface model for analysis of masonry structures. J Eng Mech 1997;123:660.

[2] Lourenço PB, Rots JG, Blaauwendraad J. Continuum model for masonry: parameter estimation and validation. J Struct Eng 1998;124:642–52.

[3] Syrmakezis CA, Asteris PG. Masonry Failure Criterion under Biaxial Stress State. J Mater Civ Eng 2001;13:58–64.

[4] Pelà L, Cervera M, Roca P. An orthotropic damage model for the analysis of masonry structures. Constr Build Mater 2013;41:957–67.

[5] Hilsdorf HK. Investigation into the failure mechanism of brick masonry loaded in axial compression. Designing, Engineering and Constructing with Masonry Products. Houston Tex.: 1969.

[6] Hamid AA, Chukwunenye AO. Compression behavior of concrete masonry prisms. J Struct Eng 1986;112:605–13.

[7] Reddy BVV, Lal R, Nanjunda Rao KS. Influence of Joint Thickness and Mortar-Block Elastic Properties on the Strength and Stresses Developed in Soil-Cement Block Masonry. J Mater Civ Eng 2009;21:535–42.

[8] Anthoine A. Homogenization of periodic masonry: plane stress, generalized plane strain, or 3D modelling? Commun Numer Methods Eng 1997;13:319–26.

[9] Berto, L., Saetta, A., Scotta, R., Vitaliani R, Berto L, Saetta A, Scotta R, Vitaliani R. Failure mechanism of masonry prism loaded in axial compression: computational aspects. Mater Struct 2005;38:249–56.

[10] Barbosa CS, Lourenço PB, Hanai JB. On the compressive strength prediction for concrete masonry prisms. Mater Struct 2010;43:331–44.

[11] Milani G, Lourenço PB, Tralli A. Homogenised limit analysis of masonry walls, Part I: Failure surfaces. Comput Struct 2006;84:166–80.

[12] Milani G, Lourenço PB, Tralli A. 3D homogenized limit analysis of masonry buildings under horizontal loads. Eng Struct 2007;29:3134–48.

[13] Furtmüller T, Adam C. Numerical modeling of the in-plane behavior of historical brick masonry walls. Acta Mech 2011;221:65–77.

[14] Schlegel R. Numerische Berechnung von Mauerwerkstrukturen in homogenen und diskreten Modellierungsstrategien. Bauhaus University, Weimar, Germany: PhD dissertation; 2004.

[15] Vyas CVU, Reddy BVV. Prediction of solid block masonry prism compressive strength using FE model. Mater Struct 2010;43:719–35.

[16] Adam JM, Brencich A, Hughes TG, Jefferson T. Micromodelling of eccentrically loaded brickwork: Study of masonry wallettes. Eng Struct 2010;32:1244–51.

[17] Brencich A, Corradi C, Gambarotta L. Compressive strength of solid clay brick masonry under eccentric loading. Proc. Br. Mason. Soc., 2002, p. 37–46.

[18] Cecchi A, Milani G, Tralli A. Validation of Analytical Multiparameter Homogenization Models for Out-of-Plane Loaded Masonry Walls by Means of the Finite Element Method. J Eng Mech 2005;131:185–98.

[19] Zucchini A, Lourenço PB. A micro-mechanical model for the homogenisation of masonry. Int J Solids Struct 2002;39:3233–55.

[20] TNO. DIANA User's Manual. Delft: TNO DIANA BV; 2012.

[21] CEN. EN 1996-1-1: Rules for reinforced and unreinforced masonry. 2005.

[22] Selby RG, Vecchio FJ. Three-dimensional Constitutive Relations for Reinforced Concrete. University of Toronto, Department of Civil Engineering; 1993.

[23] Feenstra PH. Computational Aspects of Biaxial Stress in Plain and Reinforced Concrete. Delft University of Technology, Delft, The Netherlands: PhD dissertation; 1993.

[24] Hsieh SS, Ting EC, Chen WF. A plastic-fracture model for concrete. Int J Solids Struct 1982;18:181–97.

[25] Vecchio FJ, Collins MP. The modified compression-field theory for reinforced concrete elements subjected to shear. Am Concr Inst J 1986;83:219–31.

[26] Lourenço PB, Pina-Henriques JL. Validation of analytical and continuum numerical methods for estimating the compressive strength of masonry. Comput Struct 2006;84:1977–89.

[27] Massart TJ, Peerlings RHJ, Geers MGD, Gottcheiner S. Mesoscopic modeling of failure in brick masonry accounting for three-dimensional effects. Eng Fract Mech 2005;72:1238–53.

[28] Pande G, Kralj B, Middleton J. Analysis of the compressive strength of masonry given by the equation fk = K fb^ α fm^β. Struct Eng 1994;71:7–13.

[29] Haseltine B. International Rules for masonry and their effect on the U.K. Mason Int 1987;1:41–3.

[30] Sinha BP, Hendry AW. Splitting failure of brickwork as a function of the deformation properties of bricks and mortar. Br Ceram Res Assoc Tech Note No 86 1966.

[31] Akbarzade A, Tasnimi A. Nonlinear Analysis and Modeling of Unreinforced Masonry Shear Walls Based on Plastic Damage Model. J Seismol Earthq Eng 2011;11:8–12.

[32] Drougkas A, Roca P, Molins C. Strength and elasticity of pure lime mortar masonry. Mater Struct 2015 (in press).

[33] Gumaste KS, Nanjunda Rao KS, Reddy BVV, Jagadish KS. Strength and elasticity of brick masonry prisms and wallettes under compression. Mater Struct 2007;40:241–53.

[34] Kaushik HB, Rai DC, Jain SK. Stress-Strain Characteristics of Clay Brick Masonry under Uniaxial Compression. J Mater Civ Eng 2007:728–39.

[35] Mauro A. Long Term Effects of Masonry Walls. Roma Tre University, Rome, Italy: MSc dissertation; 2007.

[36] Hossain MM, Ali SS, Azadur Rahman M. Properties of Masonry Constituents. J Civ Eng Inst Eng Bangladesh 1997;CE 28:135–55.

[37] Oliveira DV de C, Lourenço PB, Roca P. Cyclic behaviour of stone and brick masonry under uniaxial compressive loading. Mater Struct 2006;39:247–57.

[38] Panizza M, Garbin E, Valluzzi MR, Modena C. Experimental investigation on bond of FRP/SRP applied to masonry prisms. 6th Int. Conf. FRP Compos. Civ. Eng. 2012, 2012, p. 13–5.

[39] Petersen RB, Masia MJ, Seracino R. In-Plane Shear Behavior of Masonry Panels Strengthened with NSM CFRP Strips . II□: Finite-Element Model. J Compos Constr 2010;14:764–74.

[40] Vermeltfoort AT, Martens DRW, van Zijl GPAG. Brick–mortar interface effects on masonry under compression. Can J Civ Eng 2007;34:1475–85.

[41] McNary WS, Abrams DP. Mechanics of Masonry in Compression. J Struct Eng 1985;111:857–70.

[42] Mayorca P, Meguro K. Proposal for an efficient technique for retrofitting unreinforced masonry dwellings. 13th World Conf. Earthq. Eng. Vancouver, BC, Canada, August, 2004.

[43] Page AW. Finite element model for masonry. J Struct Div ASCE 1978;104:1267–85.

[44] Riddington JR, Naom NF. Finite element prediction of masonry compressive strength. Comput Struct 1994;52:113–9.

[45] Binda L, Fontana A, G. Frigerio. Mechanical behaviour of brick masonries derived from unit and mortar characteristics. 8th Int. Brick Block Mason. Conf. Vol.1, Dublin, Irel., 1988, p. 205–16.

[46] Vasconcelos G de FM de, Lourenço PB, Alves C a S, Pamplona J. Ultrasonic evaluation of the physical and mechanical properties of granites. Ultrasonics 2008;48:453–66.

[47] CEB-FIP. Model Code 1990. Thomas Telford; 1993.

[48] Chaimoon K, Attard MM. Modeling of unreinforced masonry walls under shear and compression. Eng Struct 2007;29:2056–68.

[49] Almeida JC, Lourenço PB, Barros J. Characterization of brick and brick–mortar interface under uniaxial tension. Proc. 7th Int. Semin. Struct. Masonry, Brazil CEFET-MG, 2002, p. 67–76.

[50] Khoo CL, Hendry AW. Strength tests on brick and mortar under complex stresses for the development of a failure criterion for brickwork in compression. Proc Br Ceram Soc 1973;21:57–66.

[51] Francis A, Horman C, Jerrems L. The effect of joint thickness and other factors on the compressive strength of brickwork. Proc. 2nd Int. Brick Block Mason. Conf., 1971, p. 31–7.

[52] Ohler A. Zur berechnung der druckfestigkeit von mauerwerk unter berücksichtigung der mehrachsigen spannungszustande in stein und mortel. Bautechnik 1986;63:163–8.

[53] Hendry AW. Structural masonry. Macmillan Education, Limited; 1990.

[54] ACI. ACI 530.1-11. Building Code Requirements and Specification for Masonry Structures and Related Commentaries. 2011.

[55] Como M. Statics of Historic Masonry Constructions. Springer; 2012.

Notation

E_u	Young's modulus of units
E_m	Young's modulus of mortar
E_c	Young's modulus of masonry
$f_{c,u}$	Uniaxial compressive strength of units
$f_{c,m}$	Uniaxial compressive strength of mortar
$f_{c,exp}$	Experimentally derived compressive strength of masonry
$f_{c,num}$	Numerically derived compressive strength of masonry
$f_{t,u}$	Tensile strength of units
$f_{t,m}$	Tensile strength of mortar
$f_{t,i}$	Tensile strength of unit-mortar interface

ν_u	Poisson's ratio of units
ν_m	Poisson's ratio of mortar
h_u	Height of units
l_u	Length of units
t_u	Width of units
h_m	Thickness of mortar bed joint
l_m	Thickness of mortar head joint
t_m	Thickness of transversal mortar joint
$\boldsymbol{\alpha}$	Internal damage variable vector
G_f^I	Tensile fracture energy
G_f^c	Compressive fracture energy
ε_{cr}	Crack strain
$\varepsilon_{cr,u}$	Ultimate crack strain
V	Volume of finite element
h	Characteristic element length
β	Shear retention factor
$\varepsilon_{c/3}$	Strain corresponding to one third of the uniaxial compressive strength

ε_c	Strain corresponding to the uniaxial compressive strength
ε_u	Ultimate strain for uniaxial compression
f_{c1}	Maximum principal stress
f_{c3}	Compressive failure stress
f_{cf}	Failure compressive strength
$\boldsymbol{\varepsilon}_{nst}$	Principal strain vector
$\boldsymbol{\sigma}_c$	Linear elastic stress vector
s	Linear elastic stress vector scaling factor
K_σ	Compressive strength scaling factor
ε_0	Initial strain
$\beta_{\sigma cr}$	Compressive strength reduction factor due to lateral cracking
$\alpha_{l,1}$	Lateral damage variable 1
$\alpha_{l,2}$	Lateral damage variable 2
α_{lat}	Average lateral damage variable
r	Residual strength factor
f_{P}	Peak confined compressive stress
ε_{P}	Peak confined compressive strain
ε_{U}	Ultimate confined compressive strain

f_{cr}	Residual confined compressive strength
t_n	Interface normal traction
k_n	Interface normal stiffness
Δ_n	Interface normal relative displacement
I_1	First stress invariant
J_2	Second deviatoric stress invariant

Figure Captions

Figure 1 **(a) Uniaxial compression curve and (b) compression curve under lateral compression load.**

Figure 2 **Model geometries: (a) stack bond prism, (b) running bond wall, (c) Flemish bond wall and (d) English bond column.**

Figure 3 **Three-dimensional masonry model examples under vertical load with planes of symmetry indicated. (a) finite element mesh, (b) horizontal normal stress, (c) vertical normal stress, (d) in-plane shear stress.**

Figure 4 **Experimental vs. numerical compressive strength. Coefficient of determination R^2=0.969.**

Figure 5 **Experimental vs. numerical Young's modulus. Coefficient of determination R^2=0.884.**

Figure 6 **Distribution of principal plastic strains in bed joint mortar for case S18 for increasing vertical stress levels: (a) yielding near the edge at the pre-peak range , (b) yielding extended towards the interior of the joint at peak load, (c) yielding of entire joint in the post-peak range.**

Figure 7 **Distribution of principal crack strains for case R9 for varying levels of vertical stress: (a) initial cracking in the head joints in the pre-peak range, (b) vertical cracks in the units around the bed joints at the peak load, (c) vertical cracks in the units at the post-peak range.**

Figure 8 **Experimental and numerical stress-strain diagram comparison. Numerical curves are shown in tinted lines: (a): S17 & R2** [40]**, (b): S8 & S16** [14]**, (c): S2 &S7** [32]**, (d): S13** [16]**, (e): S15** [37]**, (f): S6** [31]**.**

Figure 9 **Effect of mesh refinement for S1** [41]**: number of elements long the joint thickness.**

Table Captions

Table 1

Click here to download Table: Table 1.doc

Case	Ref.	E_u [MPa]	ν_u [-]	f_{cu} [MPa]	f_{tu} [MPa]	h_u [mm]	l_u [mm]	t_u [mm]	E_m [MPa]	ν_m [-]	f_{cm} [MPa]	f_{tm} [MPa]	h_m [mm]	l_m [mm]	t_m [mm]	$f_{c,exp}$ [MPa]	$f_{c,num}$ [MPa]	$E_{c,exp}$ [MPa]	$E_{c,num}$ [MPa]
S1	[41]	9900	0.17	44.0	1.79	55	194	89	1750	0.16	6.20	0.62	7.5	-	-	19.70	19.44	-	6456
S2	[32]	4200	0.16	23.0	3.10	45	270	135	125	{0.25}	1.25	0.19	10	-	-	12.03	10.50	729	814
S3	[33]	976	{0.15}	5.7	{0.57}	75	230	105	1500	{0.20}	1.16	{0.12}	12	-	-	1.67	2.21	467	1016
S4	[15]	14500	0.18	11.5	0.71	80	260	120	6450	0.16	3.50	{0.35}	10	-	-	6.15	6.83	-	13017
S5	[33]	3370	{0.15}	23.00	{2.30}	75	230	105	8570	{0.20}	5.14	{0.51}	12	-	-	6.70	7.40	2393	3525
S6	[31]	135	{0.15}	9.3	0.46	52	212	104	795	{0.20}	9.37	{0.94}	10	-	-	7.22	7.94	207	154
S7	[32]	4200	0.16	23.00	3.10	45	270	135	250	{0.25}	1.90	0.40	10	-	-	13.73	14.80	1181	1287
S8	[14]	5500	0.11	12.00	0.90	113	240	175	2770	0.07	4.60	{0.46}	30	-	-	4.68	5.44	4200	4702
S9	[33]	3370	{0.15}	23.00	{2.30}	75	230	105	5450	{0.20}	4.36	{0.44}	12	-	-	7.40	8.17	3135	3628
S10	[33]	976	{0.15}	5.70	{0.57}	75	230	105	238	{0.20}	0.60	{0.06}	12	-	-	1.25	2.17	379	735
S11	[15]	14500	0.18	11.5	0.71	80	260	120	6450	0.16	3.50	{0.35}	7	-	-	6.32	7.35	-	13464
S12	[15]	14500	0.18	11.5	0.71	80	260	120	6450	0.16	3.50	{0.35}	20	-	-	5.01	6.21	-	10400
S13	[16]	2000	0.10	13.8	3.30	55	250	110	1700	0.20	9.20	2.40	10	-	-	14.55	13.26	1936	1950
S14	[13]	7500	0.07	30.0	1.30	65	40	40	220	0.20	1.70	0.10	20	-	-	4.50	3.14	878	1475
S15	[37]	12000	0.20	62.6	{6.26}	45	285	130	4200	{0.20}	6.20	{0.62}	10	-	-	28.60	27.01	10000	9761
S16	[14]	5500	0.11	12.0	0.90	238	252	241	2770	0.07	4.60	{0.46}	12	-	-	8.84	6.91	5517	5330
S17	[40]	16700	0.15	66.0	1.20	52	210	100	2100	0.22	3.00	0.22	13	-	-	11.73	13.77	6800	8294
S18	[41]	9900	0.17	44.0	1.79	55	194	89	8600	0.13	21.00	2.10	7.5	-	-	34.70	36.75	-	9724
S19	[38]	5760	{0.15}	19.8	2.46	55	125	120	5490	{0.20}	2.62	0.35	10	-	-	8.24	10.31	2132	5906
S20	[41]	15000	0.13	58.9	2.74	57	200	98	11600	0.10	31.10	3.11	7.5	-	-	48.20	50.59	-	14593
S21	[33]	976	{0.15}	5.7	{0.57}	75	230	105	8570	{0.20}	5.14	{0.51}	12	-	-	1.83	4.63	365	1098
S22	[41]	15000	0.13	58.9	2.74	57	200	98	8600	0.13	21.00	2.10	7.5	-	-	40.90	44.14	-	13788
S23	[7]	8000	0.08	8.3	{0.42}	100	305	143	6600	0.19	3.45	{0.35}	30	-	-	3.10	6.57	5900	7013
S24	[13]	7500	0.07	30.0	1.30	65	40	40	220	0.20	1.70	0.10	10	-	-	9.33	5.74	1938	2380
S25	[41]	9900	0.17	44.0	1.79	55	194	89	6600	0.14	15.20	1.52	7.5	-	-	27.00	31.32	-	9342
S26	[33]	3370	{0.15}	23.0	{2.30}	75	230	105	7080	{0.20}	8.50	{0.85}	12	-	-	10.00	14.38	3700	3585
S27	[41]	15000	0.13	58.9	2.74	57	200	98	6600	0.14	15.20	1.52	7.5	-	-	32.50	37.12	-	13059
S28	[41]	9900	0.17	44.0	1.79	55	194	89	11600	0.10	31.10	3.11	7.5	-	-	37.70	43.16	-	10633
S29	[34]	5300	{0.15}	17.7	{0.89}	75	230	110	545	{0.15}	3.10	{0.31}	10	-	-	4.00	9.74	2239	3034
S30	[36]	12900	{0.15}	60.0	3.20	36	123	60	9590	{0.15}	12.00	0.97	7	-	-	18.16	24.90	8000	12601
S31	[41]	15000	0.13	58.9	2.74	57	200	98	1750	0.16	6.20	0.62	7.5	-	-	29.90	21.12	-	8063

Table 2

Click here to download Table: Table 2.doc

Case	Ref.	E_u [*MPa*]	v_u [-]	f_{cu} [*MPa*]	f_{tu} [*MPa*]	h_u [*mm*]	l_u [*mm*]	t_u [*mm*]	E_m [*MPa*]	v_m [-]	f_{cm} [*MPa*]	f_{tm} [*MPa*]	h_m [*mm*]	l_m [*mm*]	t_m [*mm*]	$f_{c,\,exp}$ [*MPa*]	$f_{c,\,num}$ [*MPa*]	$E_{c,\,exp}$ [*MPa*]	$E_{c,\,num}$ [*MPa*]
R1	[33]	3370	{0.15}	23.0	{2.30}	75	230	105	5450	{0.20}	4.36	{0.44}	12	12	-	8.20	8.47	5232	3590
R2	[40]	4000	0.13	17.0	1.00	50	206	96	1650	{0.20}	6.90	{0.69}	12.5	10	-	13.60	14.21	3200	3095
R3	[33]	976	{0.15}	5.7	{0.57}	75	230	105	238	{0.20}	0.60	{0.06}	12	12	-	1.23	1.98	580	717
R4	[33]	976	{0.15}	5.7	{0.57}	75	230	105	1500	{0.20}	1.16	{0.12}	12	12	-	1.55	2.35	735	1033
R5	[33]	3370	{0.15}	23.0	{2.30}	75	230	105	7080	{0.20}	8.50	{0.85}	12	12	-	12.60	14.40	4824	3702
R6	[33]	3370	{0.15}	23.0	{2.30}	75	230	105	8570	{0.20}	5.14	{0.51}	12	12	-	9.60	7.24	5024	3782
R7	[43]	6740	0.17	36.5	{1.50}	35	110	50	970	{0.20}	3.20	{0.32}	5	5	-	8.60	11.30	3700	3949
R8	[33]	976	{0.15}	5.7	{0.57}	75	230	105	8570	{0.20}	5.14	{0.51}	12	12	-	1.18	4.46	400	1254
R9	[44]	22000	0.15	61.0	10.70	30	105	49	8880	0.2	12.30	1.58	5	5	-	30.14	37.81	-	18540

Table 3

Click here to download Table: Table 3.doc

Case	Ref.	E_u [MPa]	v_u [-]	f_{cu} [MPa]	f_{tu} [MPa]	h_u [mm]	l_u [mm]	t_u [mm]	E_m [MPa]	v_m [-]	f_{cm} [MPa]	f_{tm} [MPa]	h_m [mm]	l_m [mm]	t_m [mm]	$f_{c,\,exp}$ [MPa]	$f_{c,\,num}$ [MPa]	$E_{c,\,exp}$ [MPa]	$E_{c,\,num}$ [MPa]
F1	[45]	4870	0.09	26.9	4.90	55	250	120	1180	0.06	3.20	0.90	10	10	10	11.00	4.29	1651	3107
F2	[45]	4870	0.09	26.9	4.90	55	250	120	5650	0.09	12.70	3.90	10	10	10	14.50	16.70	3833	5002
F3	[45]	4870	0.09	26.9	4.90	55	250	120	17800	0.12	95.00	15.70	10	10	10	17.80	29.58	4567	6390

Table 4

Click here to download Table: Table 4.doc

Case	Ref.	E_u [MPa]	v_u [-]	f_{cu} [MPa]	f_{tu} [MPa]	h_u [mm]	l_u [mm]	t_u [mm]	E_m [MPa]	v_m [-]	f_{cm} [MPa]	f_{tm} [MPa]	h_m [mm]	l_m [mm]	t_m [mm]	$f_{c,\,exp}$ [MPa]	$f_{c,\,num}$ [MPa]	$E_{c,\,exp}$ [MPa]	$E_{c,\,num}$ [MPa]
P1	[33]	3370	{0.15}	23.0	{2.30}	75	230	105	8570	{0.20}	5.14	{0.51}	12	20	20	6.70	6.65	3317	4005
P2	[33]	3370	{0.15}	23.0	{2.30}	75	230	105	5450	{0.20}	4.36	{0.44}	12	20	20	8.70	8.13	3789	3684
P3	[33]	976	{0.15}	5.7	{0.57}	75	230	105	238	{0.20}	0.60	{0.06}	12	20	20	1.46	2.07	377	690
P4	[33]	3370	{0.15}	23.0	{2.30}	75	230	105	7080	{0.20}	8.50	{0.85}	12	20	20	13.60	14.24	3677	3865
P5	[33]	976	{0.15}	5.7	{0.57}	75	230	105	1500	{0.20}	1.16	{0.12}	12	20	20	1.44	2.28	381	1056
P6	[33]	976	{0.15}	5.7	{0.57}	75	230	105	8570	{0.20}	5.14	{0.51}	12	20	20	1.38	4.13	376	1510
P7	[13]	7500	0.07	30.0	1.3	65	290	150	220	0.2	1.70	0.10	10	10	10	5.55	9.12	661	2007

Table 5

Click here to download Table: Table 5.doc

Case	Ref.	$f_{c,exp}$ [MPa]	$f_{c,Hilsdorf}$ [MPa]	$f_{c,Francis}$ [MPa]	$f_{c,Khoo\ \&\ Hendry}$ [MPa]	$f_{c,Ohler}$ [MPa]	$f_{c,Hendry}$ [MPa]	$f_{c,ACI}$ [MPa]	$f_{c,CEN}$ [MPa]	$f_{c,num}$ [MPa]
S1	[41]	19.70	24.54	29.24	19.81	17.63	9.58	11.56	12.22	19.44
S4	[15]	6.15	8.03	9.61	7.16	6.44	3.75	5.05	4.01	6.83
S8	[14]	4.68	7.79	11.36	7.21	6.50	7.93	5.16	4.50	5.44
S11	[15]	6.32	8.56	10.10	7.67	6.94	3.80	5.05	4.01	7.35
S12	[15]	5.01	6.83	8.28	6.18	5.47	3.59	5.05	4.01	6.21
S13	[31]	14.55	11.89	12.44	12.04	11.78	27.94	5.52	6.11	13.26
S14	[13]	4.50	10.96	10.88	7.99	7.12	9.97	8.76	6.34	3.14
S16	[14]	8.84	9.96	11.87	9.46	8.84	8.13	5.16	4.50	6.91
S17	[40]	11.73	15.88	14.52	12.27	10.31	6.04	15.96	13.06	13.77
S18	[41]	34.70	30.59	47.22	29.05	28.46	10.66	11.56	17.62	36.75
S20	[41]	48.20	43.23	59.75	41.25	43.50	21.17	14.54	24.32	50.59
S22	[41]	40.90	39.48	49.90	35.75	35.50	20.03	14.54	21.61	44.14
S24	[13]	9.33	15.33	15.97	10.55	10.08	12.96	8.76	6.34	5.74
S25	[41]	27.00	28.22	39.86	25.75	24.37	10.33	11.56	15.99	31.32
S27	[41]	32.50	37.33	46.29	32.37	30.56	19.53	14.54	19.62	37.12
S28	[41]	37.70	34.72	71.27	34.98	40.74	11.34	11.56	19.83	43.16
S31	[41]	29.90	33.99	39.91	25.71	23.65	18.47	14.54	14.99	21.12
R9	[44]	30.14	47.12	52.33	40.76	39.08	62.29	14.96	18.87	37.81
F1	[45]	11.00	20.24	25.85	16.28	15.77	50.70	8.14	7.10	4.29
F2	[45]	14.50	21.93	27.34	20.99	20.06	55.80	8.14	10.74	16.70
F3	[45]	17.80	36.58	35.23	76.07	-	72.91	8.14	19.64	29.58
P7	[13]	5.55	15.33	15.97	10.55	10.08	12.96	8.76	6.34	9.12

Table 6

Click here to download Table: Table 6.doc

Case	Ref.	$E_{c,\,exp}$ [MPa]	$E_{c,1D}$ [MPa]	$E_{c,EC6}$ [MPa]	$E_{c,\,num}$ [MPa]
S1	[41]	-	6351	12221	6456
S4	[15]	-	12734	4014	13017
S8	[14]	4200	4555	4500	4702
S11	[15]	-	13177	4014	13464
S12	[15]	-	11604	4014	10400
S13	[31]	-	1947	6110	1950
S14	[13]	1936	854	6340	1475
S16	[14]	5517	5251	4500	5330
S17	[40]	6800	6986	13055	8294
S18	[41]	-	9724	17622	9724
S20	[41]	-	14506	24315	14593
S22	[41]	-	13805	21613	13788
S24	[13]	1938	1386	6340	2380
S25	[41]	-	9340	15993	9342
S27	[41]	-	13066	19616	13059
S28	[41]	-	10077	19825	10633
S31	[41]	-	7977	14989	8063
R9	[44]	-	18166	18866	18540
F1	[45]	1651	3286	7101	3107
F2	[45]	3833	4971	10738	5002
F3	[45]	4567	6389	19639	6390
P7	[13]	661	1386	6340	2007

Figure 1

Click here to download Figure: figure 1

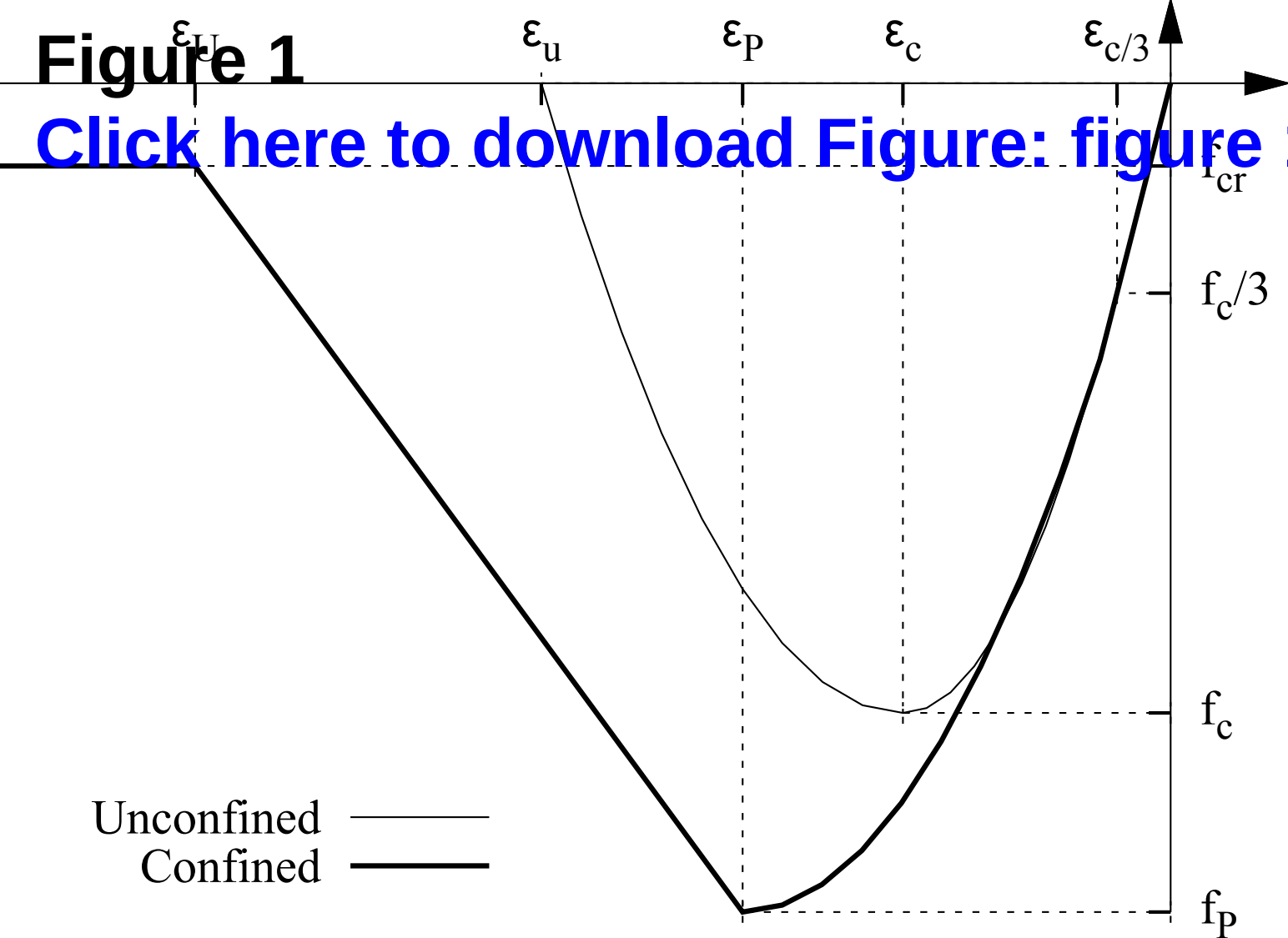

Figure 2

Click here to download Figure: figure 2.pdf

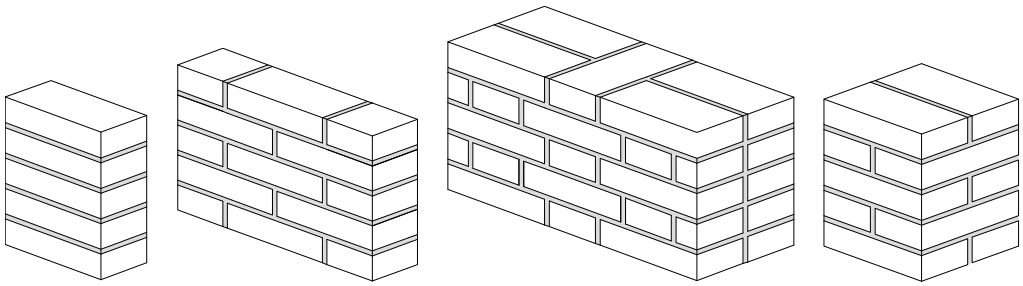

Figure 3

Click here to download Figure: figure 3.pdf

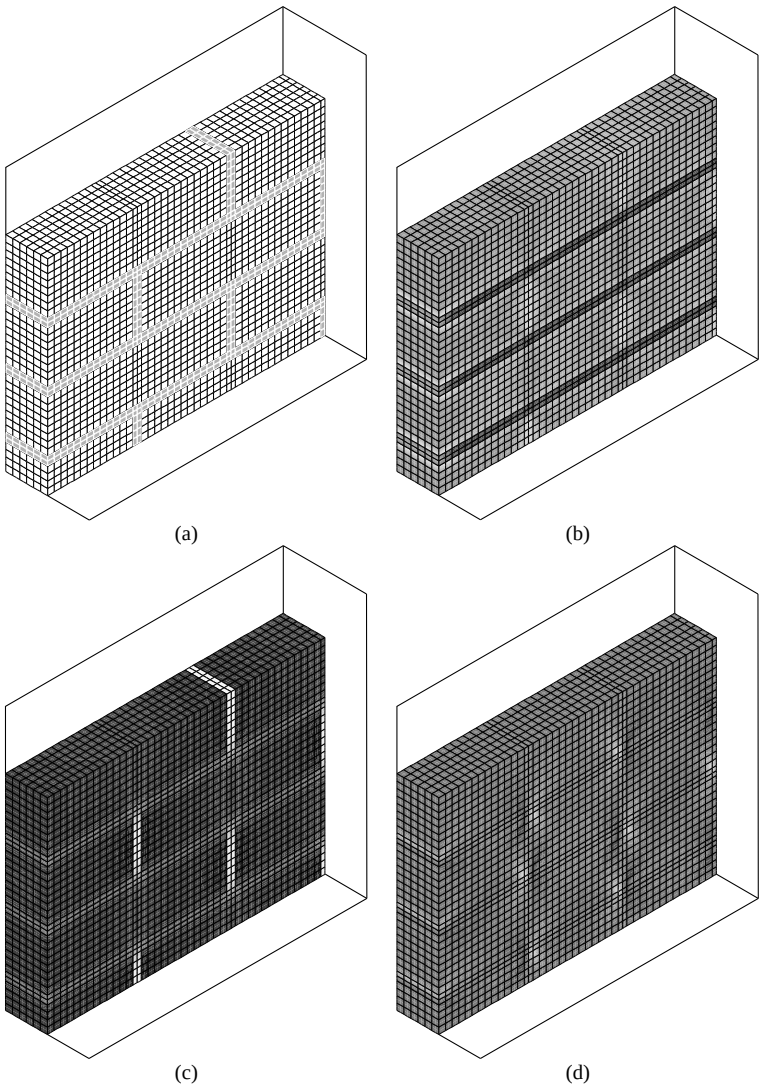

Figure 4

Click here to download Figure: figure 4.pdf

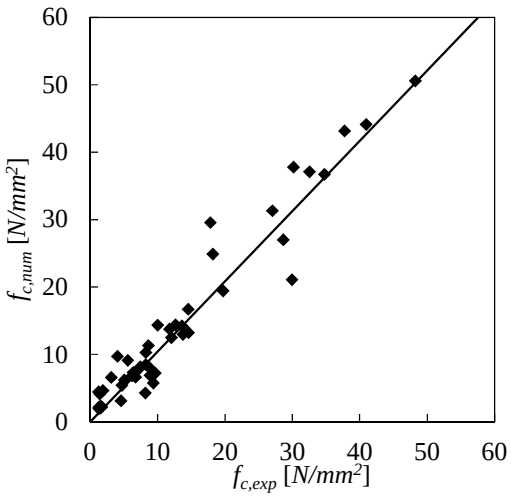

Figure 5

Click here to download Figure: figure 5.pdf

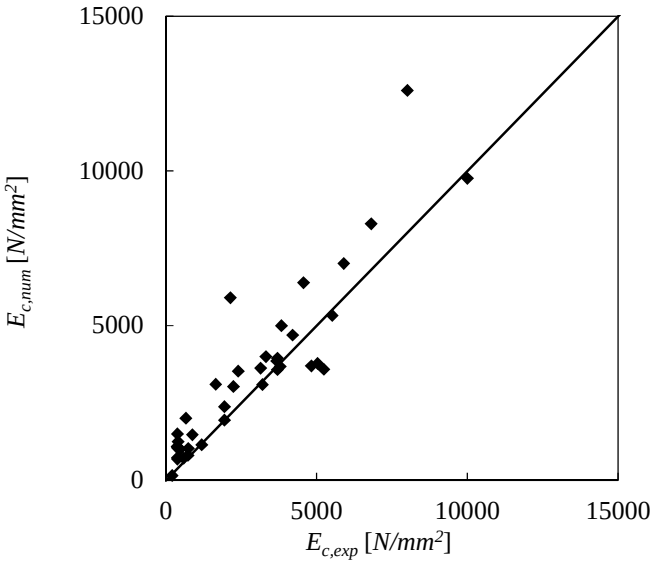

Figure 6

Click here to download Figure: figure 6.pdf

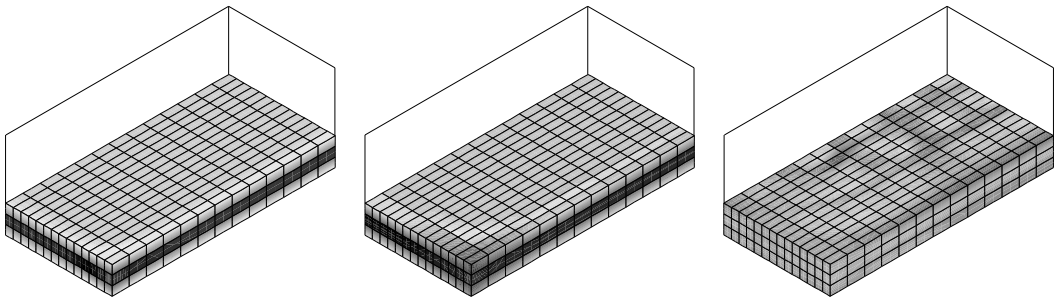

(a) (b) (c)

Figure 7

Click here to download Figure: figure 7.pdf

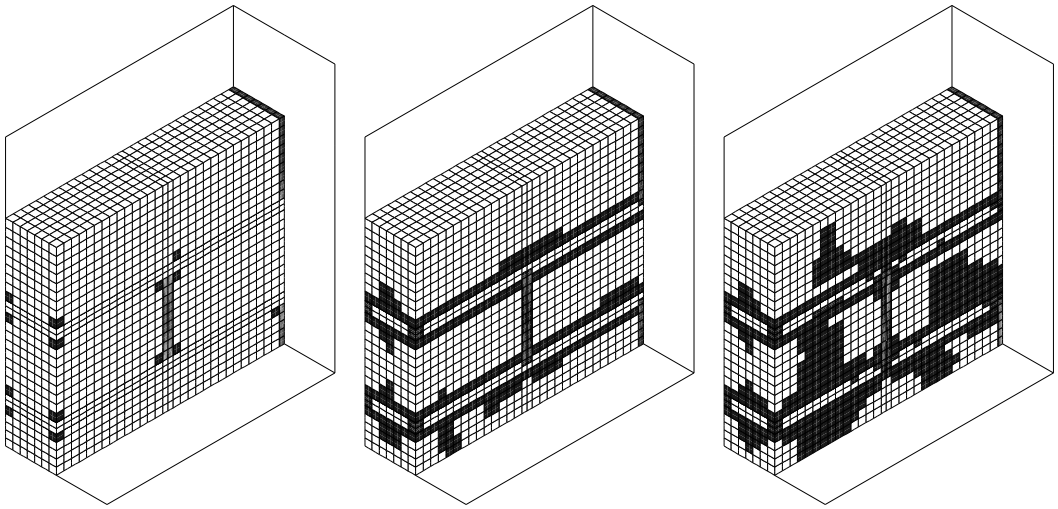

(a) (b) (c)

Figure 8

Click here to download Figure: figure 8.pdf

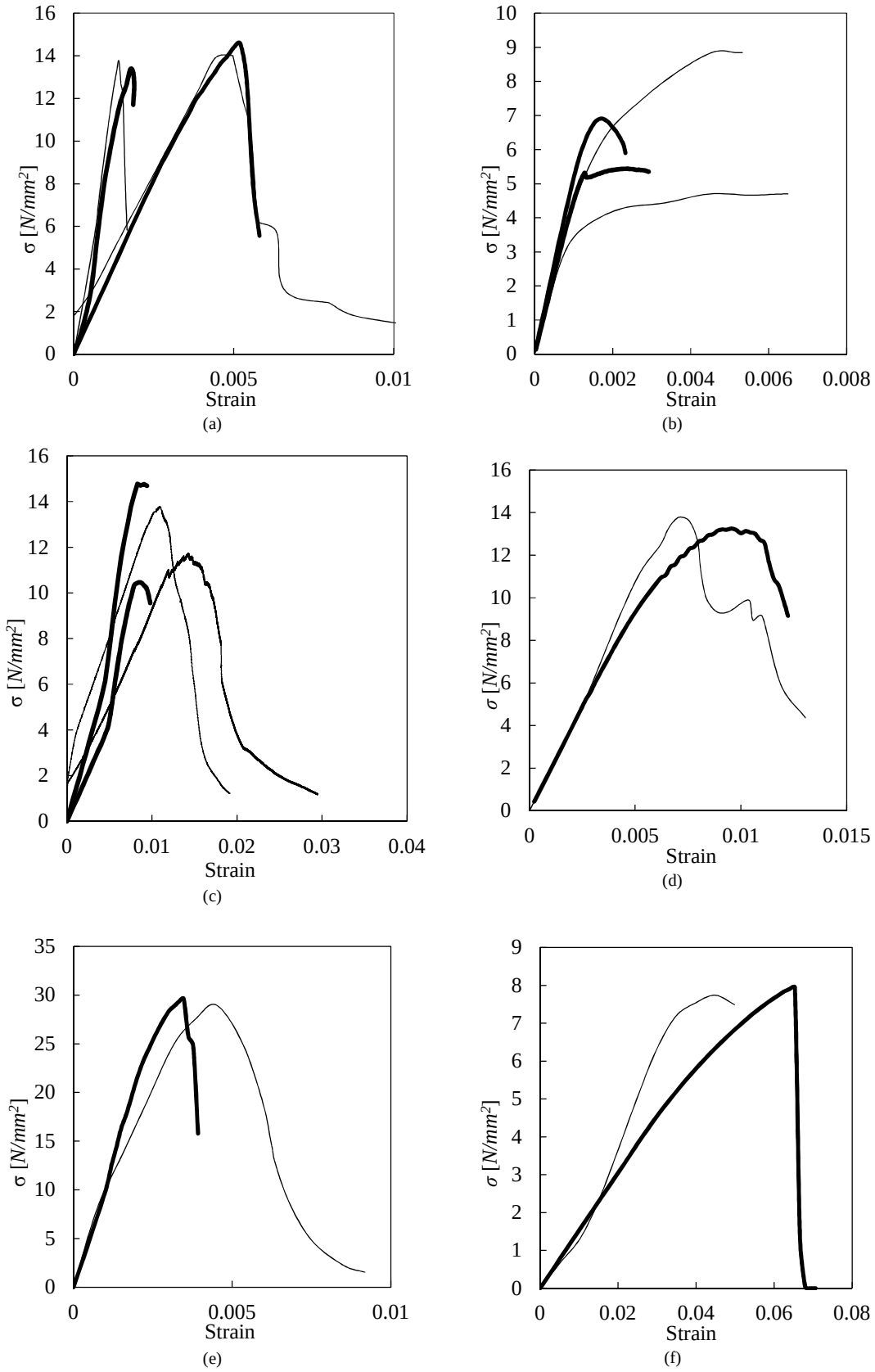

Figure 9

Click here to download Figure: figure 9.pdf